nature physics

Article

https://doi.org/10.1038/s41567-024-02641-7

Dimensional crossover in a quantum gas of light

Received: 16 January 2024

Accepted: 14 August 2024

Published online: 06 September 2024

Check for updates

Kirankumar Karkihalli Umesh [1], Julian Schulz [2], Julian Schmitt [1], Martin Weitz [1], Georg von Freymann [2,3] & Frank Vewinger [1]

The dimensionality of a system profoundly influences its physical behaviour, leading to the emergence of different states of matter in many-body quantum systems. In lower dimensions, fluctuations increase and lead to the suppression of long-range order. For example, in bosonic gases, Bose–Einstein condensation in one dimension requires stronger confinement than in two dimensions. Here we observe the dimensional crossover from one to two dimensions in a harmonically trapped photon gas and study its properties. The photons are trapped in a dye microcavity where polymer nanostructures provide the trapping potential for the photon gas. By varying the aspect ratio of the harmonic trap, we tune from isotropic two-dimensional confinement to an anisotropic, highly elongated one-dimensional trapping potential. Along this transition, we determine the caloric properties of the photon gas and find a softening of the second-order Bose–Einstein condensation phase transition observed in two dimensions to a crossover behaviour in one dimension.

In the world of many-body physics, it is common knowledge that the number of accessible dimensions profoundly influences the physical behaviour of a system, leading to the emergence of different states of matter at low dimensions (that is, fewer than three dimensions). For bosonic gases, as an example, Bose–Einstein condensation is possible in lower dimensions only for a sufficiently strong confinement of a power-law trapping potential[1]. While in two dimensions (2D) a harmonically trapped gas can undergo a phase transition to a Bose–Einstein condensate at finite temperature, this transition in one dimension (1D) is only observed with tighter confining power-law traps. When confining a 1D system within a harmonic trap, there is no sharply defined phase transition in the thermodynamic limit to the condensate phase[2], but rather a smooth crossover to a quasi-condensate. In this regime, large thermal and quantum fluctuations in one dimension inhibit the emergence of true long-range order[3,4]. For finite-size systems, the change from a phase transition in 2D to a crossover in 1D is less pronounced. Moreover, condensation can occur in 1D depending on the strength of interactions, and different regimes for quantum-degenerate Bose gases are expected[5]. It is therefore of great interest to study the crossover from three-dimensional (3D) or 2D systems to the 1D case. For ultracold atomic gases, both thermodynamic and coherence properties associated with the emergence of quasi-long range order along the dimensional crossover from three to one dimension have been studied experimentally[6,7]. In the case of a strongly interacting Bose gas, where one expects a crossover from Berezinski–Kosterlitz–Thouless-type correlations in 2D to Tomonaga–Luttinger liquid correlations[8], the interplay between interactions and dimensionality has been studied[9], and it has been observed that reducing the dimensionality can strongly influence the temperature of the system[10]. For dipolar gases, the transition to the supersolid phase has been studied along the dimensional crossover from one to two dimensions, showing a transition from a continuous to a discontinuous behaviour in the order parameter[11].

Optical quantum gases have, in recent years, emerged as an alternative platform for quantum gas experiments[12], being well-suited for the study of the dimensional crossover from 2D to 1D owing to the weak or even negligible interaction. In exciton-polariton condensates, correlations in 1D, 2D and 3D have been studied theoretically for an interacting gas[13]. Here, one crosses from long-range order in 3D via a power law in 2D to exponentially decaying first-order phase correlations in the 1D case. Experimentally, for example, the formation

[1]Institut für Angewandte Physik, Universität Bonn, Bonn, Germany. [2]Physics Department and Research Center OPTIMAS, RPTU Kaiserslautern-Landau, Kaiserslautern, Germany. [3]Fraunhofer Institute for Industrial Mathematics ITWM, Kaiserslautern, Germany. e-mail: vewinger@uni-bonn.de

https://doi.org/10.1038/s41567-024-02641-7

dynamics has been studied for 1D systems[14,15], and in 1D coupled lattices, a Kardar–Parisi–Zhang scaling for the phase has been observed[16]. In a semiconductor microcavity, the transition from 2D to 1D has been studied by varying the geometry of the drive, where the dissipative phase transition observed in 2D vanishes for a 1D drive[17].

In weakly or non-interacting photon gases, thermalization and condensation in 1D has been observed in doped optical fibres, where the photons thermally populate the longitudinal degree of freedom in a long single-mode fibre[18]. To achieve condensation, the initially linear dispersion relation is altered to a sub-linear dispersion using chirped gratings, together with a spectral filter to provide a non-trivial ground state at finite energy. In contrast to this, one can confine photons in a microcavity, effectively freezing out the longitudinal degree of freedom[19]. The transverse degrees of motion can be restricted by in-plane trapping potentials induced by transverse variations in the optical path lengths, by structuring either the cavity mirror surface[20,21] or the local refractive index[22,23]. By this, variable potential geometries can be realized, which have, for example, allowed to study the thermodynamics of 2D Bose gases that contain a few photons or are trapped in box or double well potentials[24–26]. For this system, a continuous change in the thermodynamic properties has been predicted for the harmonically trapped gas when crossing from a 2D to 1D configuration[27,28], where in contrast to the 2D case no Bose–Einstein condensation is expected[1].

Here, we use a novel technique to confine photons, namely by printing polymer structures on top of one of the cavity mirrors, which allows us to prepare structures with sizes below the wavelength of the photons. Using this method, we study the transition from two to one dimension for a harmonically trapped gas of photons by varying the aspect ratio of the trapping potential. In our system, thermalization occurs via radiative contact of the photons to a bath of dye molecules, and correspondingly the thermalization mechanism is decoupled from the dimensionality of the trapping potential, in contrast to atomic Bose gases[29,30]. For all investigated aspect ratios, a macroscopic occupation of the ground state is observed as the photon number is increased, which in two dimensions is accompanied by a sharp transition in the chemical potential, while in one dimension we observe a smooth crossover. For the intermediate cases, we observe a gradual softening of the phase transition, which can be associated to an effective (non-integer) dimension of the system.

We prepare our photon gas in an optical microcavity consisting of two highly reflective plane mirrors (reflectivity above 99.995% at 580 nm) spaced by approximately 2 µm filled with a dye solution (Fig. 1a). The confinement in the longitudinal direction effectively freezes out this degree of freedom, yielding a minimum energy of $\hbar\omega_c \approx 2.1$ eV, where ω_c denotes the low-frequency cutoff, for the photons in the cavity, corresponding to a wavelength of 580 nm. To confine the photons in the transversal direction, we printed a polymer micro-structure of height $d(x, y)$ on one of the flat mirrors. The refractive index of the polymer n_s exceeds the refractive index n of the dye solution, such that the optical path length locally increases, leading to an attractive potential energy landscape for the photons in the regions where the polymer is deposited with a potential $V \propto d(x, y)(n - n_s)/n$ (ref. 23). The geometry of the potential is determined by the geometry of the printed structure, $d(x, y)$, where the surface curvature of the printed structure translates to the curvature of the trapping potential and the absolute height to its trap depth. For the used dye solvent ethylene glycol ($n \approx 1.44$) and polymer ($n_s \approx 1.55$)[31], we find a trap depth $V \approx 1.27 k_B T$, with Boltzmann's constant k_B and the ambient temperature $T = 300$ K, for the used maximum structure height of approximately 325 nm. The polymer nanostructuring allows us to fabricate parabolic structures with sufficiently strong curvatures in the tightly confining y direction, along which the corresponding harmonic oscillator potential contains only a single bound state, rendering the photon gas system effectively one-dimensional (Fig. 1b).

The polymer structures were fabricated out of the negative-tone photoresist IP-Dip by using a direct laser writing (DLW) system

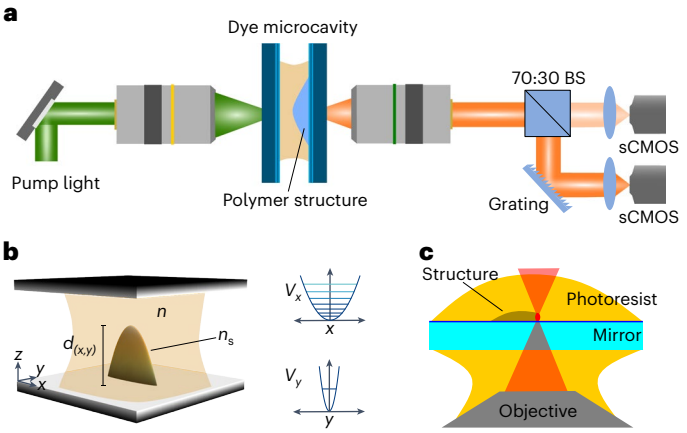

Fig. 1 | Dye-filled microcavity experimental setup and cavity mirror nanostructuring. a, The dye-filled microcavity experimental setup. The photon gas is created by pumping the intracavity dye solution using a laser beam spatially shaped using a spatial light modulator, and focused with a 10× objective into the microcavity. The cavity consists of two plane mirrors, with a polymer structure printed on one of them to provide a potential for the photons. The cavity emission is sampled using an imaging objective and subsequently analysed either spatially or spectrally. BS, beam splitter. **b**, The polymer structure (refractive index n_s) surrounded by dye solution (refractive index n) results in a potential for the trapped photon gas. **c**, The direct laser writing scheme, using a focused laser beam to polymerize the photoresist on top of the mirror surface.

(Nanoscribe Photonic Professional GT)[32]. The substrate was prepared in the immersion configuration, which means that, during the writing process, the laser was focused by the objective first through an immersion medium (in our case again IP-Dip) and the substrate of the cavity mirror and at last through the thin dielectric Bragg layers into the photoresist (Fig. 1c). The writing trajectory followed parallel lines along the longer axis of the potentials (x direction) with a line distance of 100 nm (along the y direction). To manufacture the desired potential, we print a polymer ridge with height profile $d(x, y) = h_0 - c_x x^2 - c_y y^2$, where h_0 denotes the maximum height of the structure and c_x and c_y the curvatures along x and y direction, respectively. At each point the polymer was exposed up to a height given by $d(x, y)$. For the different potentials, we keep the geometry approximately fixed along the x direction and vary the curvature along the y direction. In the following, we label the different potentials by their aspect ratio $\Lambda = \omega_y/\omega_x = \sqrt{c_y/c_x}$, with the trap frequencies ω_x and ω_y. The ratio Λ quantifies the effective dimension of the photon gas[27], where $\Lambda = 1$ corresponds to an isotropic 2D harmonic oscillator with equal trapping frequency along x and y directions (Extended Data Fig. 1), and quasi-1D is reached when the first excited mode of the strongly confined dimension is not trapped in the potential anymore (which in our case also implies $k_B T < \hbar\omega_y$), which in our case is achieved at $\Lambda \approx 22$.

To thermalize the photons, they are coupled to a thermal bath at ambient temperature $T = 300$ K, realized by a dye solution filled between the cavity mirrors (Fig. 1a), similar to previous work[19,33]. By repeated absorption–emission cycles, photons thermalize to the temperature of the dye solution, provided that thermalization is sufficiently faster than the photon losses, as is the case in our system[33–35]. Correspondingly, the photons populate the energy levels of the transversal degrees of freedom, that is, the harmonic oscillator levels in x and y direction, leading to a spectrum with equidistant frequency spacing above the lowest energy mode (called the 'cutoff' energy or frequency)[19]. As the thermalization is achieved by coupling to a bath and not by direct photon–photon collisions, we expect a thermal distribution even for a few photons, and correspondingly, for strongly confining 2D potentials, Bose–Einstein condensates with less than ten

https://doi.org/10.1038/s41567-024-02641-7

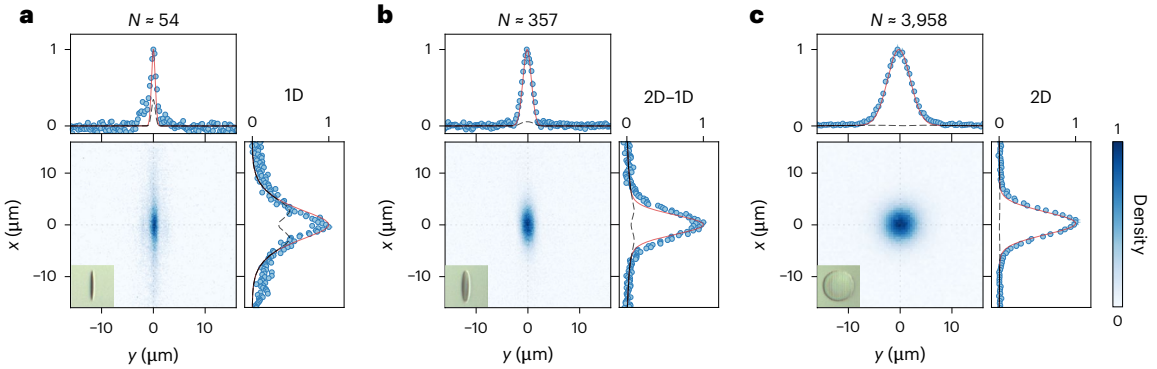

Fig. 2 | Spatial density distribution. a–c, The density distribution of photons in the quantum degenerate regime in a 1D (**a**, $\Lambda = 22$), 2D–1D (**b**, $\Lambda = 5$) and 2D (**c**, $\Lambda = 1$) harmonic oscillator potential. Insets: microscope images of the corresponding polymer structures on the cavity mirror. Dashed lines indicate the position of the cuts through the centre of the cloud along the horizontal and vertical axis shown in the side and upper panel. The dashed grey line in the cut panels shows the contribution from thermal modes, and the solid red line the contribution of the ground mode, showing the macroscopic contribution from the ground mode in all panels. For the theoretical expectations, we assume a Bose–Einstein distribution of the population within the modes, with a total photon number of $N = 54$ (1D), $N = 357$ (2D–1D) and $N = 3{,}958$ (2D). The visible deviation in the 1D case is attributed to the emission of free-space modes that are excited at the rim of the potential.

photons have been reported[24,26]. To prepare the initial photon population and to compensate for losses out of the system, we exploit the low reflectivity of our mirrors at 532 nm to inject dye molecular excitation using a laser at 532 nm, which fixes the chemical potential of the photons and thus the average total photon number N. The pump light is time modulated with a 500 ns pulse width at a 50 Hz repetition rate to prevent bleaching of the dye molecules[19]. A spatial light modulator is used to shape the pump laser profile to match the structure size on the mirror, thus reducing unwanted fluorescence from unconfined modes from outside the polymer-based structure.

To analyse the photon gas, we collect the light emitted through one of the cavity mirrors, and split the transmitted radiation into two paths after lifting the polarization degeneracy using a polarizer oriented along the polarization direction of the pump radiation, which coincides with the long axis of the 1D potential. About 70% of the light is collected by a spectrometer, and 30% is used for spatial imaging of the photon gas. Typical observed density distributions of the photon gas trapped in the 1D to 2D potential are shown in Fig. 2, and momentum space images are depicted in Extended Data Fig. 2. In the spatial distributions, one can see the density tightly squeezed along the y direction for 1D ($\Lambda = 22$), elliptic for the 1D–2D ($\Lambda = 5$) potential and radially symmetric for the isotropic 2D potential ($\Lambda = 1$). The profiles well follow expectations given by a Bose–Einstein distributed population within the bound modes of the harmonic oscillator potential. All images show data taken in the quantum degenerate regime, with a macroscopic population of the ground mode. To visualize this, the theory expectations (Methods) for ground mode (red) and thermal modes (grey dashed) are shown along with the cuts. Especially for the 1D potential, the finite size of the potential becomes visible in the diffraction pattern on the sides of the emission. Additionally, one observes a broader, smeared-out background below the sharp peak originating from trapped photons, which is attributed to residual fluorescence from free-space modes above the harmonic oscillator potential, and also to pump light scattered at the edges of the potential, which leads to an increase in emission at the edge of the potential. Those features are also present in the other cases but can be neglected owing to the larger photon numbers in the potential. As these modes can be separated spectrally, in the following we focus on the spectroscopy of the cavity emission to study the caloric properties of the gas. For this, the emission is dispersed energetically along the y direction using an optical grating and imaged onto a scientific complementary metal–oxide–semiconductor (sCMOS) camera (called 'raw spectra' in the following), which allows us to measure both the population in and the spatial profile of individual modes simultaneously. Our slitless spectrometer, which is described in more detail in the online methods, has a spectral resolution of ~0.08 THz for the lowest modes. For higher modes with quantum numbers $n_y \gg 1$, the modes start to spatially overlap, correspondingly lowering the resolution for highly excited modes. We extract a spectrum by integrating the obtained raw spectra along the non-dispersed direction, averaging over 30 realizations for a specific total photon number in 2D, over 90 in the 2D–1D case and over 120 for 1D data.

Exemplary measured spectra are shown in Fig. 3a for three different aspect ratios, together with the corresponding raw spectra in Fig. 3b obtained by dispersing the cavity emission using a grating, which retains the mode profile along the x direction. For the isotropic 2D harmonic oscillator potential with $\Lambda = 1$ (top panel), one observes equidistantly spaced modes with a frequency spacing of 0.223 THz. In the raw spectra, individual modes (n_x, n_y) with $n_x + n_y = \text{const.}$ spatially overlap, as harmonic oscillator modes with equal $n_x + n_y$ have the same energy. Correspondingly, the TEM_{00} mode can be distinguished from the group of modes TEM_{01} and TEM_{10}, but the latter two overlap. This can be seen more clearly in a linear colour scale (Extended Data Fig. 5), however there the thermal part is not visible anymore. For $\Lambda = 5$, corresponding to an anisotropic 2D harmonic oscillator potential with $\omega_y = 5\omega_x$ (middle panel), one observes equidistantly spaced modes except for the few lowest modes owing to slight distortions in the polymer structure. The mode degeneracy increases every fifth mode, as can be seen by the step-like increase in intensity at those modes. In the raw spectrum, this is reflected by the emergence of multiple parabolas corresponding to the different quantum numbers n_y along the strongly confined y direction. One correspondingly finds the emergence of the second dimension ($n_y = 1$) around the fifth mode ($n_x = 5$) along the relaxed x direction. The potential with $\Lambda = 22$ displays 1D harmonic oscillator modes (bottom panel) in the raw spectrum, with an energy spacing of 0.37 THz, and the integrated spectrum correspondingly shows discrete peaks with a degeneracy of one (see also Extended Data Fig. 3). This is characteristic for the absence of the second dimension in the recorded energy interval and which is confined by the trap for the strongly asymmetric harmonic oscillator potential, demonstrating that a photon gas trapped in this potential can be considered as being effectively 1D. The photon distribution in all three cases well follows the Bose–Einstein distribution; the grey markers in Fig. 3a indicate the expected photon distribution when neglecting the width of the individual modes. The theory estimations were calculated using a Bose–Einstein distribution $g(E)\left(\mathrm{e}^{(E-\mu)/k_\mathrm{B}T} - 1\right)^{-1}$, with the degeneracy $g(E)$. We use the energies of a quantum harmonic oscillator spectrum,

https://doi.org/10.1038/s41567-024-02641-7

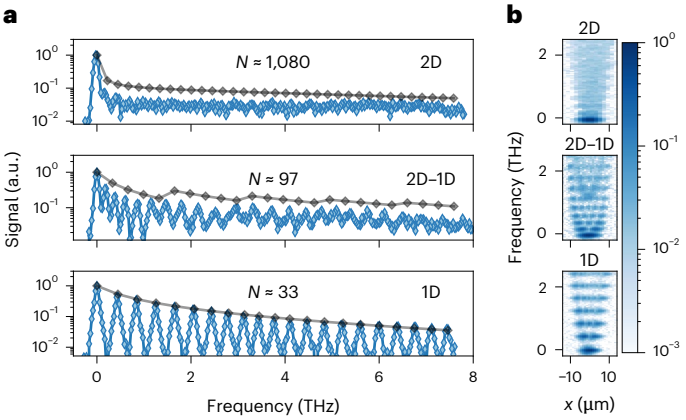

Fig. 3 | Photon gas spectroscopy. a, The integrated spectrum of the cavity fluorescence for the 2D ($\Lambda = 1$), 2D–1D ($\Lambda = 5$) and 1D ($\Lambda = 22$) harmonic oscillator potential (blue diamonds indicate measured data points, interpolated with a blue curve). The grey diamonds indicate the expected Bose–Einstein distribution of photons at $T = 300$ K, evaluated at the measured position of the harmonic oscillator modes. The grey line interpolates between these points for better visibility. **b**, Imaging the cavity emission dispersed by a grating onto a camera (raw spectra) allows one to image the shape of the first few modes. For the 2D–1D case, the energy states associated with the first excited mode of the tightly confined dimension appear at around the fifth mode. The photon number N in each case is chosen in the quantum degenerate regime, such that all modes are visible; that is, the population N_0 in the ground mode does not substantially exceed that of the excited modes, that is, $N_0/N \approx 0.3$, 0.18 and 0.3 for 2D, 2D–1D and 1D, respectively. An additional spectrum deep in the quantum degenerate regime for 1D is shown in the online methods.

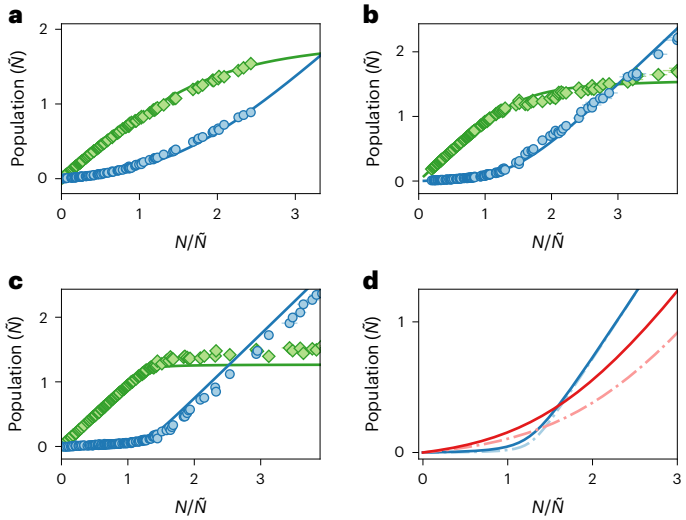

Fig. 4 | Ground versus excited mode populations. a–**c**, The population in the ground mode (blue dots) and excited modes (green diamonds) for the 1D case (**a**, $\Lambda = 22$), the 1D–2D case (**b**, $\Lambda = 5$) and the isotropic 2D potential (**c**) for a varying total number of photons. The solid lines give the theoretical expectations assuming a Bose–Einstein distribution within the modes. **d**, A comparison of the theoretical expectations for the population in the ground mode for a 1D (red) and a 2D (blue) potential with an equal number of energy levels, with trap depth of $1.2k_BT$ (solid lines) for a finite size system and a quasi-infinite system (dash-dotted lines) with a depth of $10k_BT$. One clearly observes that the effects from the finite size of the system are weaker than the effects of the dimensional crossover. For better comparison, the horizontal axis for each data set is scaled to the photon number $\tilde{N}$, with $\tilde{N} = 628$, 64 and 23 photons for the 2D, the 2D–1D and the 1D harmonic oscillator potentials (see text). Error bars showing the statistical standard deviations are on the order of the marker size. Data are presented as mean values ± s.d.

$E = \hbar\left[\omega_x n_x + \omega_y n_y + \frac{1}{2}(\omega_x + \omega_y)\right]$. The trap frequencies ω_x and ω_y are extracted from the mean mode spacing of the measured spectra, and we truncate the theoretical spectra by excluding the energy levels that exceed the trap depth inferred from the measured spectrum, and the photon number at each mode is determined by calibrating the signal from the sCMOS camera. The experimental data well follow the theoretical expectations, apart from a slightly lower mode population for the 2D case. When including the mode profile of individual modes, the measured spectrum also in this case well follows expectation for a thermal distribution at 300 K (for details, see Extended Data Figs. 4 and 5 and Methods).

Using the measured spectra, we extract the photon number in the ground mode and the excited modes, respectively, as a function of the total photon number, as shown in Fig. 4. Here, one clearly observes a smooth crossover in the ground state population for the 1D case, as expected as in 1D no phase transition to a Bose–Einstein condensate occurs. The transition becomes sharper for $\Lambda = 5$ and shows the steep increase that is associated with the phase transition for the isotropic 2D potential with $\Lambda = 1$. In the latter case, we also observe the saturation of excited modes, as expected for a phase transition from a thermal gas to a Bose–Einstein condensate. For the 1D case, the number of states bound in the potential is smaller than in the 2D case, and correspondingly the softening of the phase transition when crossing from 2D to 1D might also indicate a finite size effect. To investigate this, Fig. 4d shows the theoretical expectations for a 2D harmonic potential with the same number of energy levels as in the 1D case. While one observes a softening due to finite size effects, the effect is smaller than for the transition to 1D, and correspondingly the experimental data give evidence for the dimensional crossover from 1D to 2D. This is also visible in Fig. 3a, where no macroscopic population in the ground mode is visible.

The influence of the dimension on the phase transition can be explored by studying the order parameter when tuning the system parameters. As for our case the temperature is fixed at room temperature, the tuning parameter is the total photon number, and we use the absolute value of the chemical potential $|\mu|$ as an order parameter. To find the chemical potential μ, we first extract the internal energy from spectra as in Fig. 3 for different total photon numbers. For each spectrum, we set the ground mode energy to be the zero point energy of the harmonic oscillator, $E_0 = \hbar(\omega_x + \omega_y)/2$, count the number of photons in each energy level, multiply by the corresponding mode energy and sum over the whole spectrum, yielding the internal energy as shown in Fig. 5b. For all shown aspect ratios, the internal energy per photon, U/N, decreases for increasing photon numbers, indicating an increasing population in the low-energy states. As we do not expect a sharp phase transition in 1D (and thus no well-defined critical photon number), for better comparison, each data set is scaled to the photon number $\tilde{N}$ where the chemical potential $\mu(N)$ equals half the chemical potential at low photon number, $\mu(\tilde{N}) = \mu(N \to 0)/2$, that is, halfway between the chemical potential for the classical gas and the quantum degenerate case. We extract this number from the theoretical curves based on Bose–Einstein distributed occupations within modes (see the online methods and Extended Data Fig. 6 for details), which yields $\tilde{N} = 628$, 64 and 23 photons for the 2D, the 2D–1D and the 1D harmonic oscillator potential, respectively. In the isotropic 2D potential ($\Lambda = 1$), the curve changes slope sharply around $N/\tilde{N} \approx 1$, indicating the presence of a phase transition, while in the 1D potential ($\Lambda = 22$), the slope changes monotonically, and shows the absence of a thermodynamic phase transition. For the anisotropic 2D potential ($\Lambda = 5$), the U/N slope indeed has, although less strong, a sharp change as in the 2D isotropic potential (Fig. 5).

This is visible more strongly in the chemical potential, by numerically taking the partial derivative of the internal energy U with respect to the photon number N. The numerical derivative was done by first binning the photon number data for U (bins of photon number in a

https://doi.org/10.1038/s41567-024-02641-7

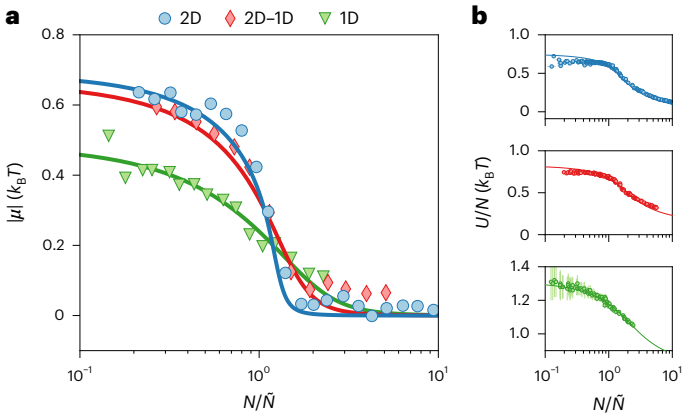

Fig. 5 | Caloric properties. The change from a phase transition in 2D to a crossover in 1D is visible in the chemical potential. **a**, The measured change (symbols) in the absolute value of the chemical potential $|\mu|$ in units of the thermal energy ($k_B T$) from 1D to 2D (1D, 2D–1D and 2D) harmonic oscillator potentials as a function of the normalized photon number $N/\tilde{N}$, where the zero point energy is set to zero, with theoretical expectations (solid curves) for corresponding harmonic oscillator potentials. **b**, The measured internal energy per particle (photon), in units of $k_B T$, (symbols) as a function of the normalized photon number $N/\tilde{N}$, for the 2D, 2D–1D and 1D harmonic oscillator potentials (from top to bottom), with their corresponding theoretical expectations (solid curves). Error bars show statistical standard deviations, and data are presented as mean values ± s.d.

geometric series spacing with a common ratio of 1.2, 1.3 and 1.2 for the 2D, the 2D–1D and the 1D harmonic oscillator potential, respectively) to suppress numerical noise (see Extended Data Figs. 7–9 for the influence of the binning). As expected, the absolute value of μ decreases for all three aspect ratios with increasing photon number. The sharp drop followed by the saturation at the ground state energy for the isotropic 2D case ($\Lambda = 1$) indicates the expected phase transition in two dimensions, while for increasing Λ we observe a gradual softening of the transition to a continuous crossover for the 1D potential. Thus, the change in the dimension of the potential from 2D to 1D leads to a crossover between the different regimes of the Bose gas instead of a sharp phase transition to a condensate phase.

To conclude, we have experimentally studied the dimensional crossover from a 2D isotropic harmonically trapped photon gas to a photon gas confined to 1D around the transition from a thermal to the quantum degenerate case. This crossover is accompanied by a softening of the phase transition, which crosses from a true second-order phase transition to a Bose–Einstein condensate in 2D to a continuous behaviour in 1D, indicated by the behaviour of the chemical potential and the internal energy of the photon gas for different photon numbers.

For the future, it will be interesting to study different trapping potentials for the photons, and investigate the spatial correlations[36]. While in 1D for the harmonically trapped system no true long-range order is possible, in our finite-size system the correlations can extend over the whole system. In the cavity platform, the losses can be tuned from a nearly lossless system to the case of a driven-dissipative condensate by modifying the low-frequency cutoff[37], which is expected to alter the correlations in the system, and additionally influence the polarization properties of the condensate[38]. Also, the structuring method presented here, based on polymer structures within the cavity, allows great flexibility in the design of potentials for photons, ranging from continuous potentials such as the ones presented here to tunnel-coupled lattice structures with large tunnelling rates. For example, potentials with a logarithmic level spacing have been proposed for factorization of large numbers[39], and in tunnel-coupled potentials, the influence of loss and drive, for example, leads to stable vortices[40,41], clustering[42] or the emergence of a Kardar–Parisi–Zhang-like scaling in the correlations[16], and for 1D chains the emergence of surface states is possible in the presence of a retarded thermooptic interaction[43].

Online content

Any methods, additional references, Nature Portfolio reporting summaries, source data, extended data, supplementary information, acknowledgements, peer review information; details of author contributions and competing interests; and statements of data and code availability are available at https://doi.org/10.1038/s41567-024-02641-7.

References

1. Bagnato, V. & Kleppner, D. Bose–Einstein condensation in low-dimensional traps. *Phys. Rev. A* **44**, 7439 (1991).
2. Ketterle, W. & van Druten, N. J. Bose–Einstein condensation of a finite number of particles trapped in one or three dimensions. *Phys. Rev. A* **54**, 656 (1996).
3. Dettmer, S. et al. Observation of phase fluctuations in elongated Bose–Einstein condensates. *Phys. Rev. Lett.* **87**, 160406 (2001).
4. Krüger, P., Hofferberth, S., Mazets, I. E., Lesanovsky, I. & Schmiedmayer, J. Weakly interacting Bose gas in the one-dimensional limit. *Phys. Rev. Lett.* **105**, 265302 (2010).
5. Petrov, D. S., Shlyapnikov, G. V. & Walraven, J. T. M. Regimes of quantum degeneracy in trapped 1d gases. *Phys. Rev. Lett.* **85**, 3745 (2000).
6. Vogler, A. et al. Dimensional phase transition from an array of 1D Luttinger liquids to a 3D Bose–Einstein condensate. *Phys. Rev. Lett.* **113**, 215301 (2014).
7. Shah, R. et al. Probing the degree of coherence through the full 1D to 3D crossover. *Phys. Rev. Lett.* **130**, 123401 (2023).
8. Yao, H., Pizzino, L. & Giamarchi, T. Strongly-interacting bosons at 2D–1D dimensional crossover. *SciPost Phys.* **15**, 050 (2023).
9. Guo, Y. et al. Observation of the 2D–1D crossover in strongly interacting ultracold bosons. *Nat. Phys.* **20**, 934–938 (2024).
10. Guo, Y. et al. Anomalous cooling of bosons by dimensional reduction. *Sci. Adv.* **10**, eadk6870 (2024).
11. Biagioni, G. et al. Dimensional crossover in the superfluid–supersolid quantum phase transition. *Phys. Rev. X* **12**, 021019 (2022).
12. Carusotto, I. & Ciuti, C. Quantum fluids of light. *Rev. Mod. Phys.* **85**, 299 (2013).
13. Chiocchetta, A. & Carusotto, I. Non-equilibrium quasi-condensates in reduced dimensions. *Europhys. Lett.* **102**, 67007 (2013).
14. Wertz, E. et al. Spontaneous formation and optical manipulation of extended polariton condensates. *Nat. Phys.* **6**, 860 (2010).
15. Wouters, M., Liew, T. C. H. & Savona, V. Energy relaxation in one-dimensional polariton condensates. *Phys. Rev. B* **82**, 245315 (2010).
16. Fontaine, Q. et al. Kardar–Parisi–Zhang universality in a one-dimensional polariton condensate. *Nature* **608**, 687–691 (2022).
17. Li, Z. et al. Dissipative phase transition with driving-controlled spatial dimension and diffusive boundary conditions. *Phys. Rev. Lett.* **128**, 093601 (2022).
18. Weill, R., Bekker, A., Levit, B. & Fischer, B. Bose–Einstein condensation of photons in a long fiber cavity. *Opt. Express* **29**, 27807 (2021).
19. Klaers, J., Schmitt, J., Vewinger, F. & Weitz, M. Bose–Einstein condensation of photons in an optical microcavity. *Nature* **468**, 545–548 (2010).
20. Kurtscheid, C. et al. Realizing arbitrary trapping potentials for light via direct laser writing of mirror surface profiles. *Europhys. Lett.* **130**, 54001 (2020).
21. Walker, B. T., Ash, B. J., Trichet, A. A. P., Smith, J. M. & Nyman, R. A. Bespoke mirror fabrication for quantum simulation with light in open-access microcavities. *Opt. Express* **29**, 10800 (2021).

22. Dung, D. et al. Variable potentials for thermalized light and coupled condensates. *Nat. Photonics* **11**, 565–569 (2017).
23. Vretenar, M., Kassenberg, B., Bissesar, S., Toebes, C. & Klaers, J. Controllable Josephson junction for photon Bose–Einstein condensates. *Phys. Rev. Res.* **3**, 023167 (2021).
24. Walker, B. T. et al. Driven-dissipative non-equilibrium Bose–Einstein condensation of less than ten photons. *Nat. Phys.* **14**, 1173–1177 (2018).
25. Busley, E. et al. Compressibility and the equation of state of an optical quantum gas in a box. *Science* **375**, 1403 (2022).
26. Kurtscheid, C. et al. Thermally condensing photons into a coherently split state of light. *Science* **366**, 894 (2019).
27. Stein, E. & Pelster, A. Thermodynamics of trapped photon gases at dimensional crossover from 2d to 1d. *New J. Phys.* **24**, 023013 (2022).
28. Stein, E. & Pelster, A. Photon BEC with thermo-optic interaction at dimensional crossover. *New J. Phys.* **24**, 023032 (2022).
29. Kinoshita, T., Wenger, T. & Weiss, D. S. A quantum Newton's cradle. *Nature* **440**, 900–903 (2006).
30. Mazets, I. E., Schumm, T. & Schmiedmayer, J. Breakdown of integrability in a quasi-1D ultracold bosonic gas. *Phys. Rev. Lett.* **100**, 210403 (2008).
31. Gissibl, T., Wagner, S., Sykora, J., Schmid, M. & Giessen, H. Refractive index measurements of photo-resists for three-dimensional direct laser writing. *Opt. Mater. Express* **7**, 2293 (2017).
32. Hohmann, J. K., Renner, M., Waller, E. H. & von Freymann, G. Three-dimensional μ-printing: an enabling technology. *Adv. Opt. Mater.* **3**, 1488 (2015).
33. Klaers, J., Schmitt, J., Damm, T., Vewinger, F. & Weitz, M. Bose–Einstein condensation of paraxial light. *Appl. Phys. B* **105**, 17 (2011).
34. Kirton, P. & Keeling, J. Thermalization and breakdown of thermalization in photon condensates. *Phys. Rev. A* **91**, 033826 (2015).
35. Schmitt, J. et al. Thermalization kinetics of light: from laser dynamics to equilibrium condensation of photons. *Phys. Rev. A* **92**, 011602 (2015).
36. Damm, T., Dung, D., Vewinger, F., Weitz, M. & Schmitt, J. First-order spatial coherence measurements in a thermalized two-dimensional photonic quantum gas. *Nat. Commun.* **8**, 158 (2017).
37. Öztürk, F. E. et al. Observation of a non-Hermitian phase transition in an optical quantum gas. *Science* **372**, 88 (2021).
38. Moodie, R. I., Kirton, P. & Keeling, J. Polarization dynamics in a photon Bose–Einstein condensate. *Phys. Rev. A* **96**, 043844 (2017).
39. Gleisberg, F., Mack, R., Vogel, K. & Schleich, W. P. Factorization with a logarithmic energy spectrum. *N. J. Phys.* **15**, 023037 (2013).
40. Gladilin, V. N. & Wouters, M. Vortices in nonequilibrium photon condensates. *Phys. Rev. Lett.* **125**, 215301 (2020).
41. Gladilin, V. N. & Wouters, M. Vortex-pair annihilation in arrays of photon cavities. *Phys. Rev. A* **105**, 013527 (2022).
42. Panico, R. et al. Onset of vortex clustering and inverse energy cascade in dissipative quantum fluids. *Nat. Photonics* **17**, 451–456 (2023).
43. Calvanese Strinati, M., Vewinger, F. & Conti, C. Nonlocality-induced surface localization in Bose–Einstein condensates of light. *Phys. Rev. A* **105**, 043318 (2022).

Methods

DLW of the polymer structures

DLW is an established fabrication method in which a laser is focused into a photosensitive material, which usually initiates a polymerization reaction[32]. However, the energy of one photon is not sufficient to excite the photosensitive material. By using a femtosecond-pulsed laser and strong focusing, the high field strength at the focal point can lead to the 'simultaneous' absorption of two photons. Owing to this two-photon process, the excitation only takes place in the volume around the focal point. This also means that, in contrast to other lithography methods, this fabrication method is not bound by the Abbe limit, as only above a certain threshold is the intensity high enough to start a polymerization reaction. If enough polymerization reactions are started in a given volume, the polymers will tangle up or crosslink and form a solid piece of polymer. For the photoresist we used typically, a minimum polymerized volume (voxel) has diameters of 100 nm (x,y) and 250 nm (z). More important for the structures in this manuscript, however, is the precision with which the laser focus can be positioned relative to the substrate, as this limits the surface accuracy. In our case, this is done via three capacitively controlled piezoelectric stages (in x, y, z), each reaching in closed-loop operation nanometre precision. After the writing process, the excess liquid photoresist is removed with solvents (propylene glycol monomethyl ether acetate and isopropanol) and only the solid structures remain.

To demonstrate that we can indeed fabricate structures using DLW with the needed surface accuracy, Extended Data Fig. 1 shows exemplary atomic force microscopy measurements of one polymer structure for an isotropic potential. The difference between the programmed shape and the measured height profile is smaller than 100 nm everywhere, except on the edges of the structure. This verifies that we can indeed fabricate structures with the lower of the trap frequencies as designed. We can also fabricate the steeper trap with higher trap frequencies accurately (in the squeezed y direction), as can be seen from the fact that, in the spectra, the eigenenergies correspond to the predicted energies for the corresponding ratio of the trap frequencies.

Preparation of the photon gas

Cavity construction. The used experimental apparatus is similar to as described in earlier works (see refs. 19,33 for details). The cavity is built with two plan mirrors with reflectivity above 99.995%, with nanostructured potentials on the surface of one of the mirrors, spaced by ~1.4 µm. The mirrors are placed on mirror mounts with piezoelectric tilt adjustment, which in turn are mounted on a three-axis stage for cavity alignment. One of the mirrors is mounted on a piezo stage for fine adjustment of the cavity length (along the z axis) to tune the cavity cutoff. The mirrors are brought close to each other, and a drop of dye solution containing 1 mmol concentration of Rhodamine 6G in ethylene glycol is added, and held in place by surface tension. Further reduction in cavity length is done using the piezo stage until the longitudinal mode number q, is constrained by $q < 12$, which assures that other longitudinal cavity modes are not excited by the fluorescence of the dye and correspondingly the photon gas effectively becomes two dimensional. The dye molecules are excited using a pump laser beam cavity at 0° incidence. The laser beam at 532 nm wavelength is chopped in time into 500 ns pulses with a 50 Hz repetition rate to prevent bleaching as well as heating of dye molecules. The pump light is shaped spatially with a high-power spatial light modulator to match the profile of the polymer structures.

In the cavity, the dispersion relation due to the short mirror spacing is modified with respect to free space and acquires quadratic, that is, massive particle-like, character. The transverse TEM_{00} mode of the parabolic potentials becomes the lowest populated eigenmode, which acts as a low-frequency cutoff at energy $\hbar\omega_c = hc/\lambda_c$, where λ_c, h and c are the cutoff wavelength, Planck's constant and speed of light in vacuum, respectively. This energy corresponds to a photon rest mass of $m = \hbar\omega/(c/n)^2$, where c denotes the speed of light and $n \approx 1.43$ is the refractive index of the solvent ethylene glycol. For such a system, it is known that a Bose–Einstein condensate exists at thermal equilibrium conditions for a 2D harmonic potential[33].

Thermal equilibrium of photons in the cavity is achieved as the photons are absorbed and re-emitted many times by the dye molecules, provided the dye fulfils the Kennard–Stepanov relation, which is the case for Rhodamine 6G to good accuracy. The conversion of photons into dye electronic excitations and vice versa induce a thermal spectral distribution of the photon gas at the temperature of the dye rovibrational excitations, which are at room temperature. Given that thermal emission is negligible in the limit of $\hbar\omega_c \gg k_\mathrm{B}T$, temperature and chemical potentials are independently tunable. This is a striking difference to the usual case of black-body radiation where photons vanish in the system walls upon lowering the temperature instead of exhibiting condensation. In our experiment, the chemical potential of the photons (and correspondingly the photon number) is determined by the ratio between excited and ground state molecules, which is set by the power of the pump laser. Assuming equal statistical weights of the rovibronic manifold in ground and excited molecular states, one can express the chemical potential of the photons via

$$\mathrm{e}^{\frac{\mu}{k_\mathrm{B}T}} = \frac{M_\uparrow}{M_\downarrow}\mathrm{e}^{\frac{\hbar(\omega_{\mathrm{ZPL}}-\omega_c)}{k_\mathrm{B}T}},$$

where $M_\uparrow$ and $M_\downarrow$ denote the population in the molecular excited and ground state, respectively, $\hbar\omega_c$ is the low-energy cutoff and $\hbar\omega_{\mathrm{ZPL}}$ is the energy of the zero phonon line of the used dye[33]. We note that, owing to the coupling to the bath, also small ensembles of photons can exhibit a thermal distribution. As the temperature (and thus the spectral distribution) are imprinted by the dye solution, in principle a single photon can (on average) show thermal properties, and for the case of a few photons this has been demonstrated experimentally[22,24,26].

The repeated absorption–emission cycles can be seen as an exchange of both energy and particles, thus the dye acts as a reservoir in the grand canonical sense. This can lead to grand canonical fluctuations in the photon number. However, in our experiment, we average over multiple realizations, and correspondingly those fluctuations are averaged out. Additionally, the fact that the photons are coupled to a heat bath implies that thermalization is decoupled from the photon number or the dimension. This is in contrast to, for example, atomic Bose gases, where thermalization occurs via particle–particle collisions and thus only slow or even no thermalization occurs for low particle number or in 1D, where the system becomes integrable[29,30].

Theoretical modelling

Bose–Einstein distribution. To calculate the spectral and spatial distribution of the photon gas trapped in a dye microcavity, we calculate the bound energy levels ϵ_i and their degeneracy g_i for the given potential. The required trapping frequencies ω_x and ω_y as well as the trap depth are inferred from the measured spectra, and compared with the design parameters. Using the measured energy levels, we calculate the spectral photon distribution using a Bose–Einstein distribution

$$N_i = \frac{g_i}{\exp\left(\frac{\epsilon_i-\mu}{k_\mathrm{B}T}\right)-1},$$

where the chemical potential μ is calculated using the measured total photon number N via $N = \sum \frac{g_i}{\exp\left(\frac{\epsilon_i-\mu}{k_\mathrm{B}T}\right)-1}$. Correspondingly, there are no free parameters; the theoretical expectation is completely determined by measured parameters. The corresponding theoretically expected ground state population $N_0 = \frac{g_0}{\exp\left(\frac{\epsilon_0-\mu}{k_\mathrm{B}T}\right)-1}$ and the excited state population $N_{\mathrm{excited}} = \sum_{i\neq 0}\frac{g_i}{\exp\left(\frac{\epsilon_i-\mu}{k_\mathrm{B}T}\right)-1}$ for given total photon number N can then be determined.

Summing over the bound energy levels weighted with the corresponding occupation gives the expected internal energy $U = E_{\mathrm{rest}} + \sum \epsilon_i N_i$, where $E_{\mathrm{rest}} = \frac{mc^2}{n^2}$ is the effective rest energy of the photons.

The chemical potential is extracted from the internal energy by taking the partial derivative of U with respect to the total photon number N, that is, $\mu = \frac{\partial U}{\partial N}$. For better comparison, we set the energy of the ground state to zero; that is, the chemical potential approaches zero for large photon number in all cases (Fig. 5a).

Spatial density distribution. For the spatial distribution, we assume wavefunctions of the quantum harmonic oscillator

$$\psi_i(x) = \frac{1}{\sqrt{2^n n!}} \left(\frac{m\omega_x}{\pi\hbar}\right)^{1/4} \exp\left(-\frac{m\omega_x x^2}{2\hbar}\right) H_n\left(\sqrt{\frac{m\omega_x}{\hbar}}x\right) \quad .$$

We then take the outer product of the wavefunctions along x and y directions and square it to get the density of each mode. The total density distribution is calculated by summing over all modes weighted with the calculated mode occupancy N_i,

$$\Psi = \sum |\psi_i(x)\psi_i^*(y)|^2 N_i \quad .$$

For the excited modes, we use a similar approach to give

$$\Psi_{\mathrm{excited}} = \sum_{i\neq 0} |\psi_i(x)\psi_i^*(y)|^2 N_i \quad ,$$

which gives the spatial density distribution of only the excited states. The effective photon mass $m = 2\pi\hbar n^2/(\lambda_c c)$ is determined by the known cutoff wavelength λ_c (which in our case is ~580 nm) and the refractive index n of the dye solution.

Determining the crossover point $\tilde{N}$. While for 2D the critical point for the phase transition is well defined, in 1D, where a true phase transition is absent, a definition for a critical photon number is not possible. To compare the different potentials, we determine a crossover point at which $\mu(N) = \mu(N \to 0)/2$ using the theoretical expectations for the corresponding potentials. In the classical regime, that is, for small photon number, the chemical potential approaches a constant value, while in the quantum degenerate regime the chemical potential approaches zero. Correspondingly, the midpoint between these extremes indicates the crossover from classical to quantum degenerate.

Interestingly, the crossover point $\tilde{N}$ is close to the photon number at which the theoretical expectation for U/N changes its slope in a double log plot, as shown in Extended Data Fig. 6. For small photon number, we expect a Boltzmann-like behaviour for the classical photon gas, while quantum statistics is expected as soon as the coherence length is on the order of the size of the potential. Correspondingly, the inner energy changes its slope. To determine the crossover point, we fit a straight line to the linear part of the curve to either side of the change of curvature, and the intersection point of these two straight lines is found to be 611, 63 and 19 photons for the 2D, 2D–1D and 1D potentials, respectively. We want to emphasize that other definitions for the crossover point are also valid. As both theory and experiment are scaled by the same factor, this only leads to a horizontal shift of all curves in the logarithmic plots.

Spectroscopy of the photon gas

Cavity fluorescence. The cavity fluorescence is captured by an objective; after filtering out the pump light, the light passes through a polarizer aligned to the polarization of the ground mode. As our system is driven-dissipative, the ground mode (with the fastest emission time scale) is slightly polarized, with a preferred direction along the pump light polarization, while thermal modes are unpolarized[38]. The light is then split into two arms: 70% of the light is guided to the spectrometer, while the remaining 30% is imaged onto a sCMOS camera to measure density profiles. In the spectrometer arm, the light is expanded in the Fourier plane onto the grating, and the dispersed light is then imaged onto the sCMOS camera using a spherical lens.

To calibrate the photon number we, replace the cavity mirror pointing away from the spectrometer by the output of an optical fibre connected to a tunable dye laser. From the known power at the fibre output and the measured signal on the spectrometer camera, we can determine the transmission function of our setup. We do this for different wavelengths within the spectrum of our photon gas, and extrapolate between those points using the known mirror transmission. By this, we can calculate the photon number for each measured spectrum.

Momentum space distribution. Additionally to the spatial distributions, we can also image the momentum space distribution of our photon gas. Exemplary distributions are shown in Extended Data Fig. 2 for the 2D and 2D–1D case, both in the classical and in the quantum degenerate regime. Similar to the real space distributions in Fig. 2, the distributions well follow the theoretical expectations. Outside the potential, one also observes residual fluorescence from free-space modes not confined by the potential. As expected for harmonic trapping, the momentum space images are rotated by 90° with respect to the real space images for the 1D–2D case; that is, the spatially confined direction has a broader momentum space distribution, both for the thermal part and for the ground mode.

Spectrum analysis. The spectrometer first expands the light in the Fourier plane onto the grating, and the dispersed light is then imaged onto the sCMOS camera using a spherical lens. One exemplary spectrum of the cavity fluoresce for the 1D potential is shown in Extended Data Fig. 3. The dispersion is along the horizontal axis, and owing to the slitless nature of the spectrometer, the mode profiles are preserved along both vertical and horizontal axes (Extended Data Fig. 3a). By integrating the raw spectrum image along the vertical axis and applying the transmission correction explained above, we obtain processed spectra as shown in Extended Data Fig. 3b. This spectrum is a convolution of the spectral information and the (horizontal) spatial profile of the different modes. While the low energy modes can be resolved individually, for the higher energy modes this convolution leads to a 'smearing out'. Thus, to extract the temperature, one needs to compare the convoluted spectra with the measured data, which in our case well agrees to a Bose–Einstein distribution at a temperature of 300 K (Extended Data Fig. 4).

This convolution between spectral and spatial information can be solved by either using a diffusor or an Ulbricht sphere in front of the spectrometer to destroy the spatial information, or by tomography using a moving slit in front of the spectrometer. However, owing to the weak signal for the 1D potential, this is not feasible in our current setup.

Extended Data Fig. 5 shows an exemplary spectrum for the 2D case with a linear colour scale. While the thermal tail is barely visible in the linear scale, one can clearly observe that the lowest modes are well separated and do not overlap. The Gaussian profile of the ground mode is visible, while the higher modes are degenerate $n_x + n_y = \mathrm{const.}$; that is, mutliple modes overlap spatially, and their shape is correspondingly not observable.

Extraction of thermodynamic quantities. The internal energy U is measured by multiplying the integrated spectrum with the corresponding energy and then summing over the product. In Extended Data Figs. 7–9, the grey data points correspond to the measured energies U/N, and it is apparent that the data points have high frequency noise that would lead to high numeric noise (when taking the numerical derivative) for the evaluation of the chemical potential μ. To mitigate

this, we binned the data points (U) into bins spaced in a geometric series; to demonstrate the binning effects, data binned with three different common ratios are shown in blue, green and red in Extended Data Figs. 7–9. In the second row, the corresponding chemical potential $|\mu|$ extracted from the binned data is plotted along with theoretical expectations (solid black curve). The binning indeed influences the amount of noise in the chemical potential $|\mu|$ but does not substantially change the phase transition or crossover features. The smaller bin sizes (smaller common ratio) enhance the numerical noise (blue data points) for all potentials, whereas larger bin sizes (larger common ratio) reduce the numerical noise but result in only a few data points (red data points). Hence, we choose bin sizes with a common ratio between these two extremes for our analysis.

Data availability

The data presented in this manuscript are available via Zenodo at https://doi.org/10.5281/zenodo.10571407 (ref. 44). Source data are provided with this paper.

References

44. Karkihalli Umesh, K. et al. Dimensional crossover in a quantum gas of light: datasets. *Zenodo* https://doi.org/10.5281/zenodo.10571407 (2024).

Acknowledgements

We acknowledge valuable discussions with E. Stein and A. Pelster. This work has been supported by the Deutsche Forschungsgemeinschaft through CRC/Transregio 185 OSCAR (project no. 277625399, all authors). We acknowledge financial support by the EU (ERC, TopoGrand, 101040409, J.Schmitt), by the DLR with funds provided by the BMWi (grant no. 50WM2240, F.V. and M.W.) and by the Cluster of Excellence ML4Q (EXC 2004/1-390534769, M.W. and J. Schmitt).

Author contributions

G.v.F., J. Schulz, K.K.U. and F.V. conceived and designed the experiment. J. Schulz performed the nanofabrication. K.K.U. designed and performed the experiment. K.K.U., J. Schulz and F.V. analysed the data. J. Schmitt and M.W. contributed materials/analysis tools. All authors discussed the results. K.K.U., J. Schulz and F.V. wrote the initial paper. All authors contributed to the critical review of the paper.

Competing interests

The authors declare no competing interests.

Additional information

Extended data is available for this paper at https://doi.org/10.1038/s41567-024-02641-7.

Supplementary information The online version contains supplementary material available at https://doi.org/10.1038/s41567-024-02641-7.

Correspondence and requests for materials should be addressed to Frank Vewinger.

Peer review information *Nature Physics* thanks Arturo Camacho-Guardian and the other, anonymous, reviewers for their contribution to the peer review of this work.

https://doi.org/10.1038/s41567-024-02641-7

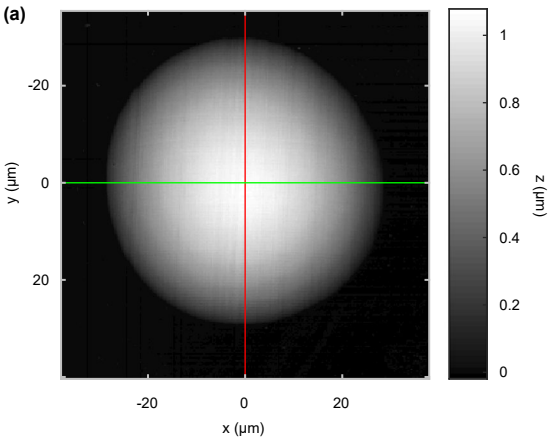

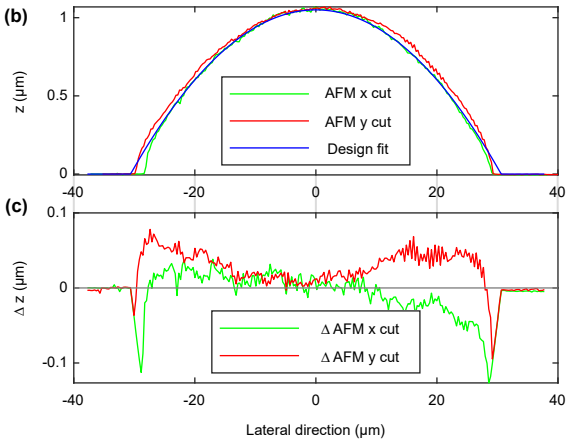

Extended Data Fig. 1 | Nanostructure surface profile. a, AFM measurement of the surface of a printed isotropic paraboloid. **b** Sections through the AFM data as marked in (**a**) along the x axis (green) and the y axis (red) compared to a parabola with the curvature programmed for the 3D print (blue). **c** Difference of the programmed height profile and the measured height profile of the printed structures.

https://doi.org/10.1038/s41567-024-02641-7

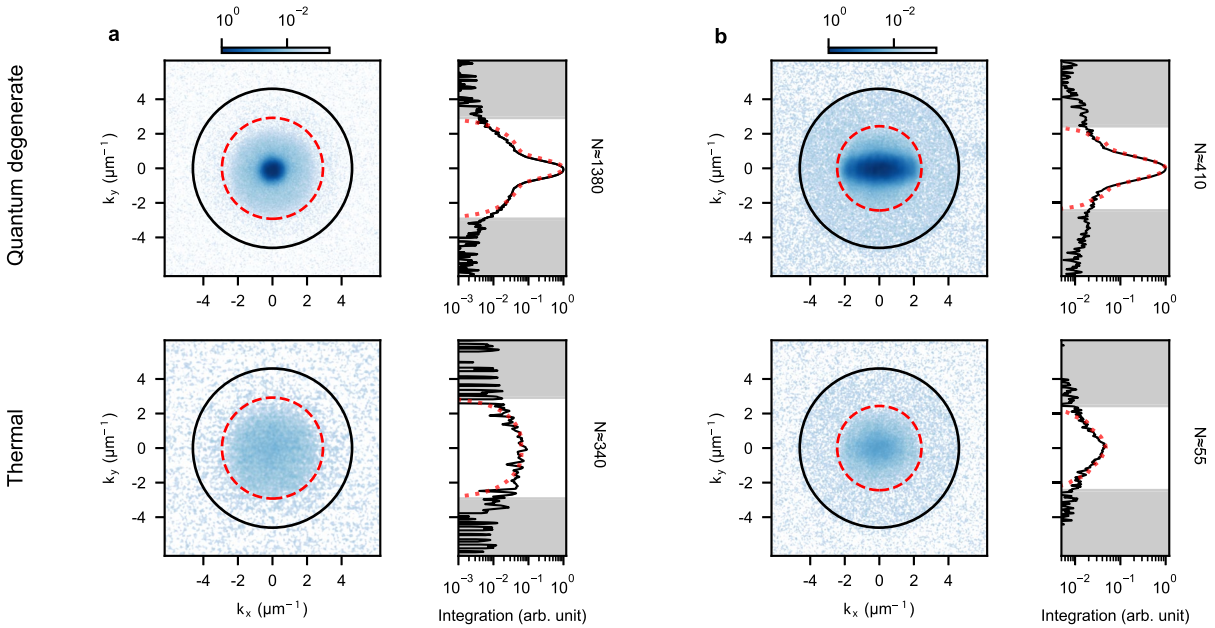

Extended Data Fig. 2 | Momentum space distributions. Exemplary momentum space distributions of the cavity fluorescence for the 2D (panel **a**) and the 2D-1D case (panel **b**) in the thermal (that is classical) and quantum degenerate regime. The red dashed circle denotes wavevectors with $k_x^2 + k_y^2 = 2mV/\hbar^2$, and the black circle the numerical aperture of the imaging system. The side panels show distributions integrated along the k_x direction, together with the corresponding expectation as a red dotted line. The broad distribution extending to regions with wavevectors which cannot be trapped by the potential (indicated by the grey shaded areas) is attributed to the emission from free-space modes not confined in the potential.

https://doi.org/10.1038/s41567-024-02641-7

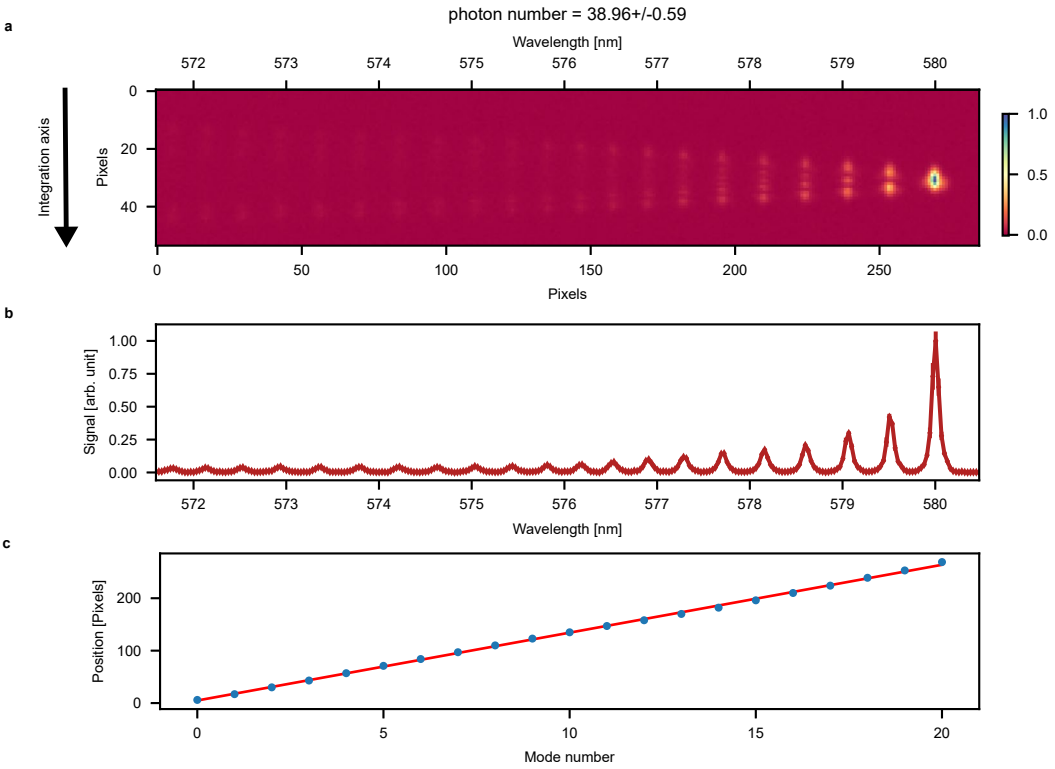

Extended Data Fig. 3 | Spectum Analysis. Exemplary spectrum of the cavity fluorescence for the 1D case. **a**, raw image of the spectrum on the spectrometer camera, the vertical axis is the spatial axis and the horizontal axis is both the (compressed) spatial and dispersive axis. The integration is along the vertical axis as marked by the arrow. **b**, the integrated, transmission-corrected spectrum, in a linear scale. Panel **c** shows the position of the observed modes from **b** as a function of the mode number. As expected for a harmonic oscillator potential, we observe a linear increase in mode energy with the mode number.

https://doi.org/10.1038/s41567-024-02641-7

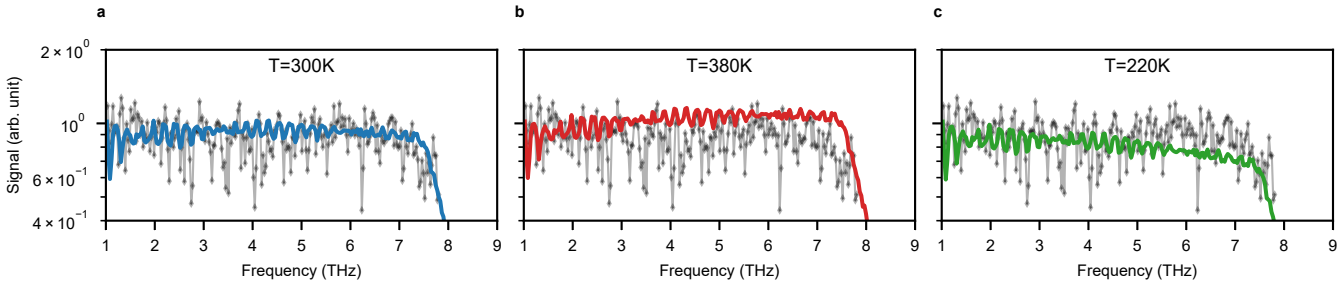

Extended Data Fig. 4 | Thermal tail temperature. Comparison of the thermal tail of the measured spectrum in the 2D case, together with the theoretical expectation, convoluted with the mode profiles for a temperature of 300K (panel **a**), 380 K (panel **b**) and 220 K (panel **c**), respectively. The data is the same as shown in Fig. 3a, note that only the thermal modes with energies at least $h \times 1$THz above the ground mode are shown. The good agreement shows that our photon gas within uncertainties can be described by a room temperature distribution.

https://doi.org/10.1038/s41567-024-02641-7

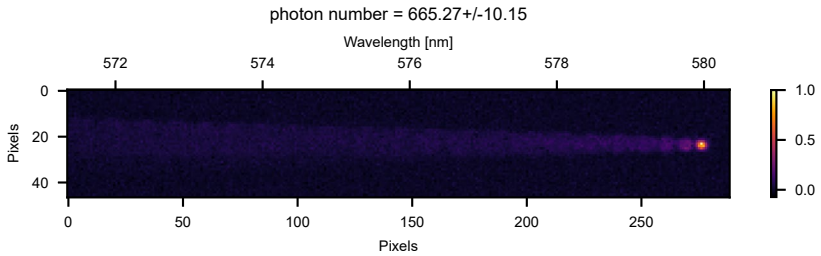

Extended Data Fig. 5 | Raw spectrogram for the 2D potential. Exemplary spectrum of the cavity fluorescence. In contrast to the main text, the raw spectrum for the 2D potential is here shown using a linear scale color map.

https://doi.org/10.1038/s41567-024-02641-7

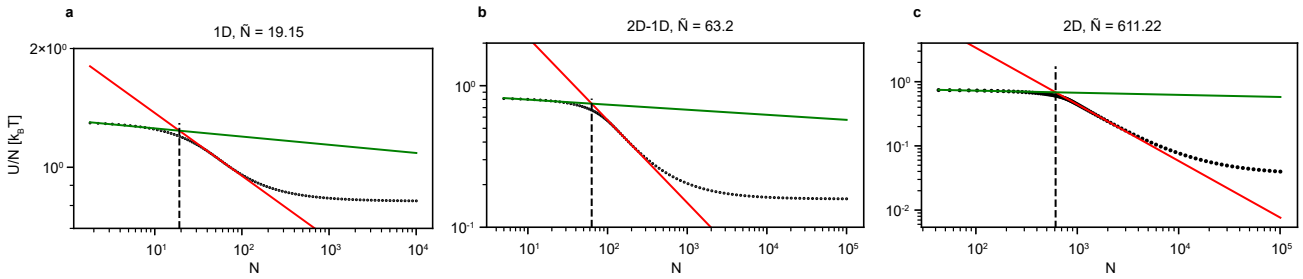

Extended Data Fig. 6 | Alternative definition of $\tilde{N}$. Double log plot of the theoretically expected inner energy U/N as a function of photon number N (black points) for 1D (**a**), 2D-1D (**b**) and 2D (**c**). The green and red lines are fits in the linear regions before and after the curve starts changing slope. The photon number where both lines intersect is indicated by the black dashed line. This number is determined to be $\tilde{N} = 19$ (**a**), $\tilde{N} = 63$ (**b**), and $\tilde{N} = 611$ (**c**).

https://doi.org/10.1038/s41567-024-02641-7

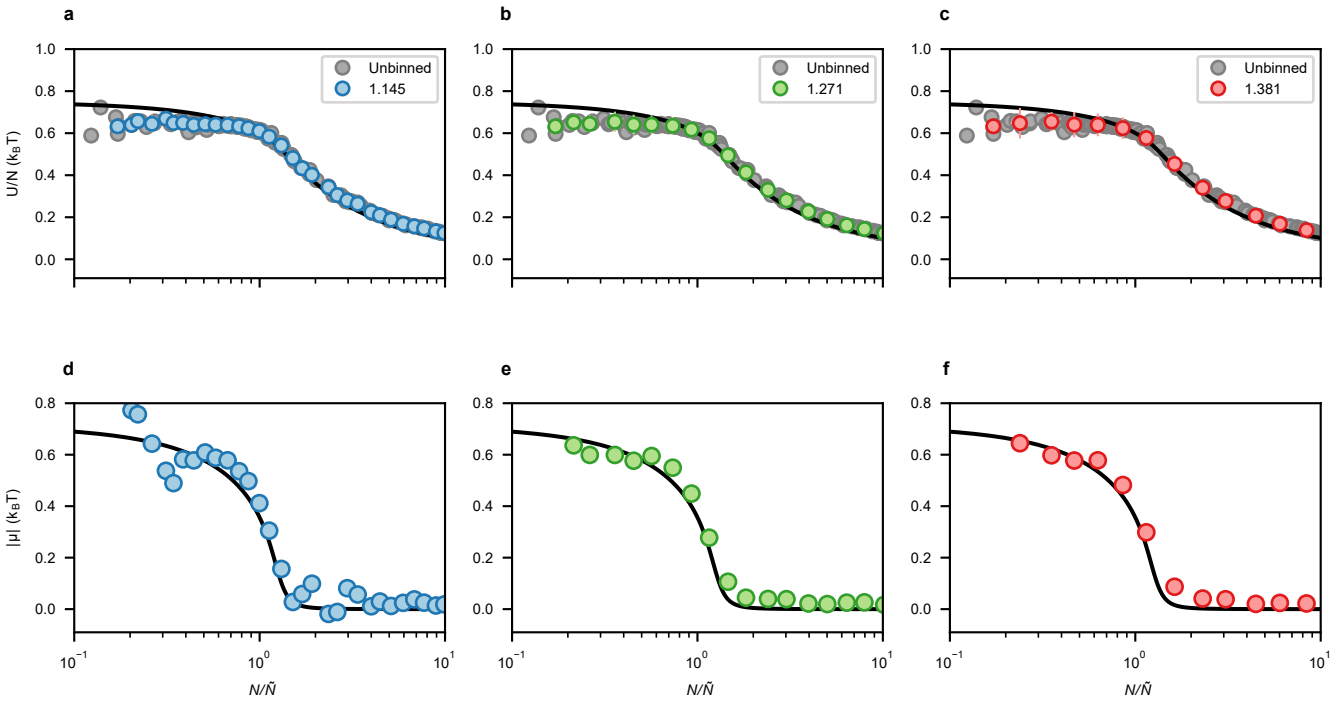

Extended Data Fig. 7 | Binning effects on caloric properties for the 2D potential. Binning effects on U/N and $|\mu|$ for the 2D potential. **a**–**c**, The mean value of the unbinned internal energy per particle U/N is plotted in grey in the upper row with corresponding theoretical expectations in the black solid curve. Binned data as mean values +/- SD with a geometric series spacing with common ratios 1.145, 1.271 and 1.381 are plotted in blue, green and red in three separate columns. **d**–**f**, Corresponding data for the chemical potential $|\mu|$ (symbols) is plotted in the lower row with corresponding theoretical expectations in the black solid curve.

https://doi.org/10.1038/s41567-024-02641-7

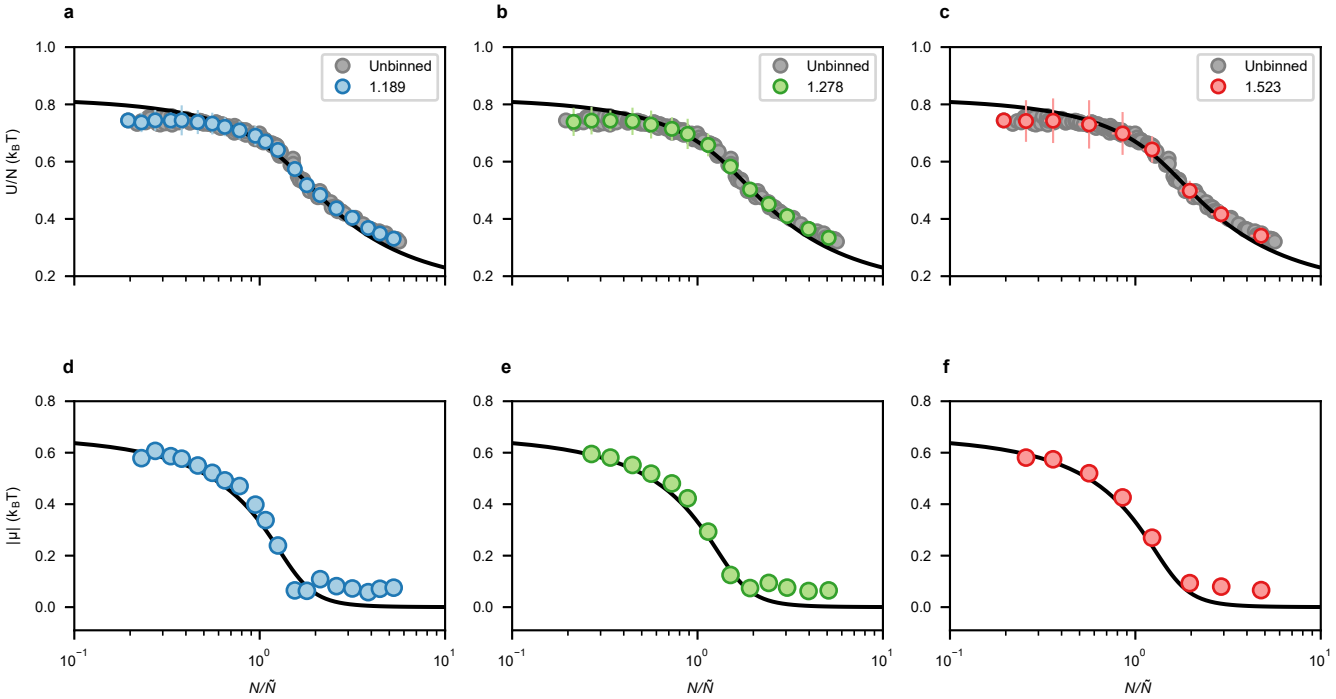

Extended Data Fig. 8 | Binning effects on caloric properties for the 2D-1D potential. Binning effects on U/N and $|\mu|$ for the 2D-1D potential. **a**–**c**, The mean value of the unbinned internal energy per particle U/N is plotted in grey in the upper row with corresponding theoretical expectations in the black solid curve. Binned data {as mean values +/- SD} with a geometric series spacing with common ratios 1.189, 1.278 and 1.523 are plotted in blue, green and red in three separate columns. **d**–**f**, Corresponding data for the chemical potential $|\mu|$ (symbols) is plotted in the lower row with corresponding theoretical expectations in the black solid curve.

https://doi.org/10.1038/s41567-024-02641-7

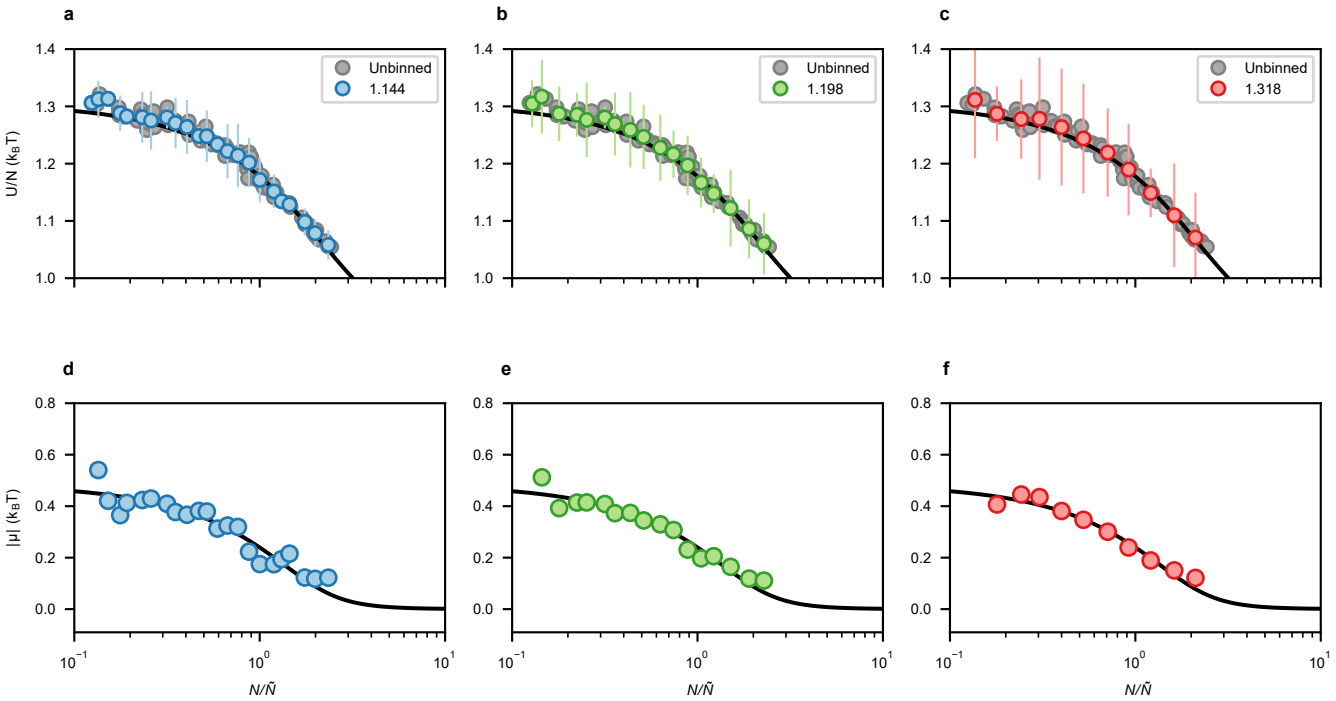

Extended Data Fig. 9 | Binning effects on caloric properties for the 1D potential. Binning effects on U/N and $|\mu|$ for the 1D potential. **a**–**c**, The mean value of the unbinned internal energy per particle U/N is plotted in grey in the upper row with corresponding theoretical expectations in the black solid curve. Binned data {as mean values +/- SD} with a geometric series spacing with common ratios 1.144, 1.198 and 1.318 are plotted in blue, green and red in three separate columns. **d**–**f**, Corresponding data for the chemical potential $|\mu|$ (symbols) is plotted in the lower row with corresponding theoretical expectations in the black solid curve.